Final Technical Report

Electrochemically-Driven Phase Transformations in Battery Compounds

Award Number: DE-SC0014435

Project Period: 09/15/2015 - 09/14/2018

Principal Investigator: Ming Tang

Performing Organization: Rice University, Houston, TX 77005

Funding Office: Basic Energy Sciences, Physical Behavior of Materials

Table of Contents

Abstract

Ion-insertion compounds for advanced batteries frequently exhibit phase transformations as the concentration of the working ion varies. Under the large electrochemical driving forces inherent to practical use, systems are often driven far from equilibrium and exhibit phase transition behavior not seen in other materials. An improved understanding of phase transformation pathways in electrode materials upon cycling will lead to new materials design concepts and electrochemical duty cycle management strategies that improve capacity utilization at high charge/discharge rates, reduce voltage and capacity hysteresis, and extend battery life. The main goal of this project is to develop a predictive understanding of the phase transition behavior of battery compounds when electrochemically driven far from equilibrium through a combined experimental-theoretical approach. Research focuses on elucidating how the phase transition behaviors in a diverse group of selected model systems (olivines, lithium metal, etc.) are regulated by various factors including transformation strains, plasticity, metastable transformation pathways, electrode microstructure, surface reaction and ion diffusion kinetics, and what are the unique features of phase transitions in battery compounds. To this end, operando X-ray-based characterization techniques are applied to interrogate the structure and composition evolution of electrode materials and interfaces at nano- and meso-scales. Mesoscale modeling techniques such as phase-field simulation are employed to shed light on the experimental observations and establish a unified framework for describing phase transition behaviors in battery compounds.

Introduction

The importance of low-cost, high performance electrical energy storage to accelerate deployment of electric vehicles and stationary storage for grid-connected and off-grid renewable energy is now widely recognized. Amongst numerous storage technologies being explored, electrochemical storage (batteries) remains the most promising approach for meeting the energy density thresholds that will enable widespread adoption of electric transportation. For stationary storage, advanced batteries have also emerged as the dominant technology, an example being the California Public Utilities Commission's mandate to deploy 1.3GW of storage by 2020, equivalent to 5-6 GWh of batteries. Although batteries are complex systems consisting of many components with specific functions, the fundamental enabler of any battery system remains the storage electrode materials that define the voltage, capacity, energy, power, and life of the battery through their physical properties.

A unifying central theme that has emerged from recent research advances for the physical behavior of storage electrode materials is that ion storage compounds are inherently used, and routinely driven, *far-from-equilibrium*. This is increasingly true with the drive towards new materials of higher storage capacity, power, and energy density. The fundamental reasons behind such demanding utilization are not difficult to appreciate. Consider, for example, that a Li-ion battery operates under at least a substantial driving force of 4 eV per Li^+ ion, and that the composition swings widely to exchange at least one out of every seven atoms (e.g., $Li_{0.5}CoO_2$, $LiFePO_4$, $LiMn_2O_4$) and as high as four out of every five atoms (e.g., $Li_{4.4}Si$). Smaller composition excursions are not interesting from a capacity/energy viewpoint. Furthermore, these large excursions in composition and high driving forces all are imposed at or near room temperature, often delaying or preventing thermal equilibrium. Examples of far-from-equilibrium behavior include the solid-state-amorphization of Si upon initial lithiation at room temperature[1]. All current examples of Si anodes including those recently reaching commercialization utilize the amorphous domain of behavior. Another electrode material in which nonequilibrium behavior has been elaborated in detail include $LiFePO_4$, the prototypical phospho-olivine cathode, in which the thermodynamically preferred first-order phase transition is circumvented in various ways under dynamic use conditions, including solid solution or noncrystalline disorder transformations[2-11]. As we show, olivine materials remain an ideal research platform for nonequilibrium behavior with emergence of new compositions and phases. Furthermore, replacing the graphite anode with Li metal in commercial Li-ion batteries has been recognized as a key strategy to enable next-generation high-energy rechargeable batteries. However, Li metal anode faces the long-standing problem of *dendrite growth* during electroplating under far-from-equilibrium conditions (e.g. high current density), which results in inferior cycle life and safety issues[12-15]. This is another outstanding example of where the nonequilibrium phase transition behavior makes tremendous impact on the advancement of energy storage technology.

Our goal of achieving fundamental understanding of the far-from-equilibrium behavior of battery electrode materials under electrochemical driving forces directly addresses a Grand Challenge in the 2007 Grand Challenges report stated as: "How do we characterize

and control matter away - especially very far away - from equilibrium?". This project also lies squarely within two of the main themes identified in the 2015 Grand Challenges study, which are: "Mastering Hierarchical Architectures and Beyond-Equilibrium Matter" and "Beyond Ideal Materials and Systems: Understanding the Critical Roles of Heterogeneity, Interfaces and Disorder." Within this framework, our objective is to conduct studies on model systems that will: 1) Systematically characterize and model each of the possible non-equilibrium responses that solid compounds may exhibit in response to electrochemical stimuli; and 2) Allow prediction of the type of non-equilibrium response by establishing design, usage, or materials selection rules. Specifically, we focus in this project on phase transitions in model systems lithium and sodium phospho-olivines and lithium metal as representatives of electrode compounds of qualitatively different characteristics. Working with the research group of Dr. Yet-Ming Chiang at MIT in this collaborative project, research was conducted to provide valuable insights on the interrelations between *transformation strains, plasticity, metastable transition pathways, electrode microstructure, competition between surface reaction and diffusion kinetics,* and how they collectively determine the phase transition behaviors in the systems studied.

Research Accomplishments Resulting from this Project

I. Effect of transformation strain on phase transition behavior

In collaboration with Dr. Yet-Ming Chiang's group, we investigated the nonequilibrium response of model systems of low and high electrochemical strains, illustrated in Figure 1. In the Li-phospho-olivine system Li(Mn,Fe)PO_4, the transformation strain can be tuned over a range from ~1 vol% to ~6.5 vol% by varying the transition metal ratios, as a consequence of which distinctly different responses are obtained as discussed below. Plasticity plays a relatively minor role in these crystal systems at transformation strains below ~5%. At the other extreme, under the previous award we also studied lithiated Si, in which the electrochemical strain exceeds 300% and amorphization is an established response. In this case plastic deformation of the resulting alloy dominates the response to electrochemical strain. We showed that this response and can be controlled in a manner that dictates the anisotropy and uniformity of electrochemical expansion and can mitigate mechanical failure[16,17].

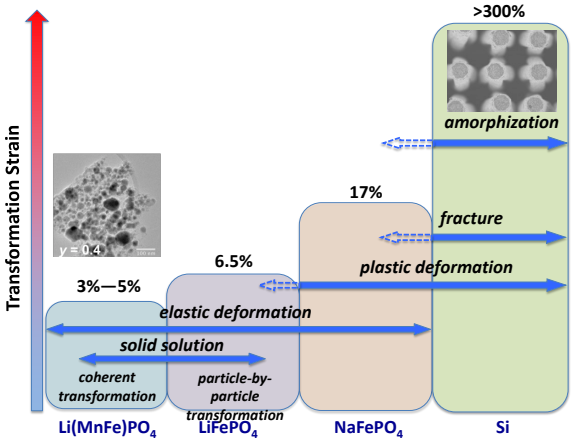

Figure 1. Systems studied, corresponding transformation strains, and nonequilibrium responses observed.

The intermediate regime of transformation strain in Figure 1 is exemplified by $NaFePO_4$ (NFP) olivine, a new cathode compound with technological potential for sodium ion batteries. This compound's 17 vol% transformation strain is one of the largest amongst alkali ion intercalation cathodes. The material behavior in this intermediate strain regime, where plasticity must be included, is studied in this project. It is shown below that a unique and remarkable disordering response to electrochemical lithiation occurs in nanoscale NFP as a new strain accommodation mechanism.

Li(Mn_yFe_{1-y})PO_4 phospho-olivines:

The phospho-olivine family $AMPO_4$ (A=Li, Na and M=Fe, Mn, Ni, Co), spans a wide range transformation-induced misfits, with free-strain values varying from as low as 1 vol% for $LiMn_{0.4}Fe_{0.6}PO_4$ to 6.5 vol% for $LiFePO_4$ to 17 vol% for $NaFePO_4$. Experiments which revealed that room temperature phase transitions occur by quite different mechanisms as the transformation strain increases. $LiMn_yFe_{1-y}PO_4$ (LMFP) is the second-generation olivine of greatest commercial interest due to its higher voltage and power. *Operando* SR-PXD shows a continuous transformation path through metastable solid solutions and phases[18], see Figure 2. We determined precisely the unit cell parameters of all crystalline phases during electrochemical titration, and find within the LMFP compositions three features that indicate nonequilibrium behavior: (a) During two-phase coexistence, the lattice dimensions, and therefore composition, of one or both phases change continuously, in violation of the Gibbs equilibrium phase rule; (b) Significant hysteresis is observed between charge and discharge in the compositions of phases at the same overall Li concentration (i.e., state-of-charge), and clearly both cases cannot represent the equilibrium condition; (c) The boundaries between phase fields (e.g., single and two-phase fields) differ between charge and discharge, and from literature phase diagrams[19,20]. From these results, it became clear that nano-LMFP does not follow the "binary particle" model of nano-LFP cycled at low rates[21] but instead exhibits continuous transitions within single particles. This behavior is attributed to a thermodynamic tendency to minimize coherency strain energy. LMFP is unique in that the nonequilibrium solid solutions are stable for long periods (at least days) and occur uniformly throughout the material. This is explained by the low misfit strain between phases producing low coherency strain energy.

We subsequently utilized the tunable strain of LMFP to answer a key question: *Does low transformation strain, or access to a coherent phase transition, correlate to the exceptional power performance of olivines such as LMFP?* As showed in ref. [18], LMFP delivers higher capacity at the C-rates above 10C than does nano-LFP. For this reason LMFP is of current commercial interest for high power Li-ion batteries for microhybrid (start-stop operation) and HEV applications, where its advantages over LFP are especially apparent at low use temperatures. Upon applying detailed *operando* structure analyses to samples of a range of Mn content from y = 0 (pure LFP) to y = 0.8, e.g. y = 0.4 (Figure 2) and y = 0.2 (Figure 3b), a clear correlation is observed. Each LMFP composition has two first-order transitions according to the equilibrium phase diagrams[19] corresponding to the Fe^{2+}/Fe^{3+} couple and the Mn^{2+}/Mn^{3+} couple, with an intermediate solid solution phase existing between the endmembers. In Figure 3a, the broad maximum for high C-rate correlates with small misfit strains (<3 vol%). The y = 0.2 composition

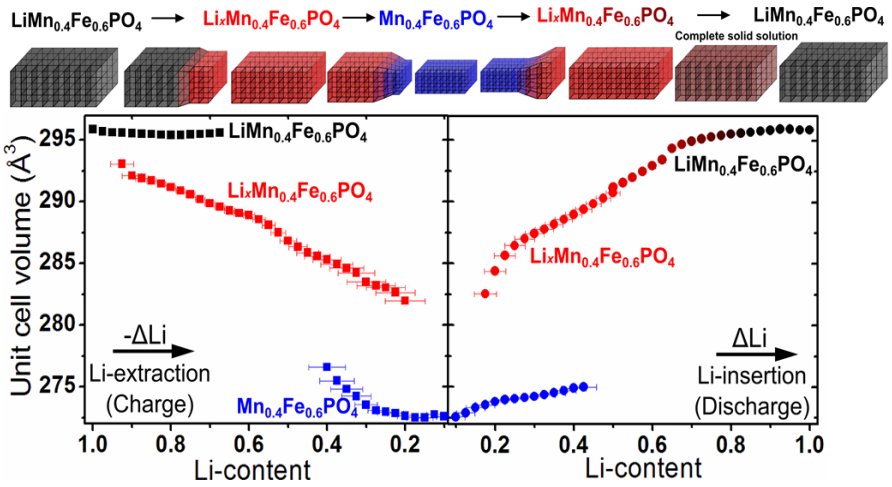

Figure 2 Unit cell volumes determined by Rietveld refinement of operando SR-PXD data measured during Li extraction (charge) and insertion (discharge) at a C/10 rate of LMFP (52 nm particles), supporting a coherent transformation model as shown at top. Sample has 52nm average crystallite size. From ref. [18].

near the maximum is unique in that the first order transition is completely bypassed during (non-equilbrium) discharge (Figure 3b) but not charge. While transformation strain plays an important role in suppressing phase separation, quantitative prediction of the optimal composition and rate capability of LMFP is non-trivial. Our experience with modeling LFP shows that the phase boundary orientation and hence misfit strain vary with discharge/charge rate, and complete solid solution behavior only occurs above an overpotential of ~80mV when the elastic energy penalty associated with the large misfit strain of (010) phase boundary can be overcome. Furthermore, the effect of coherency strain on the rate capability of LMP has two opposing effects: while it thermodynamically reduces or eliminates the two-phase co-existence region, kinetically it represents an energy barrier to phase transition and Li intercalation. Therefore an optimal transformation strain exists, which is both material and rate dependent, to maximize rate performance. Our phase-field model of LFP[22] can be extended to LMP to predict the relation between coherency strain, the ability to bypass first-order transition and the Li intercalation kinetics in this system, and to provide useful insights on how to optimize material compositions for different application conditions.

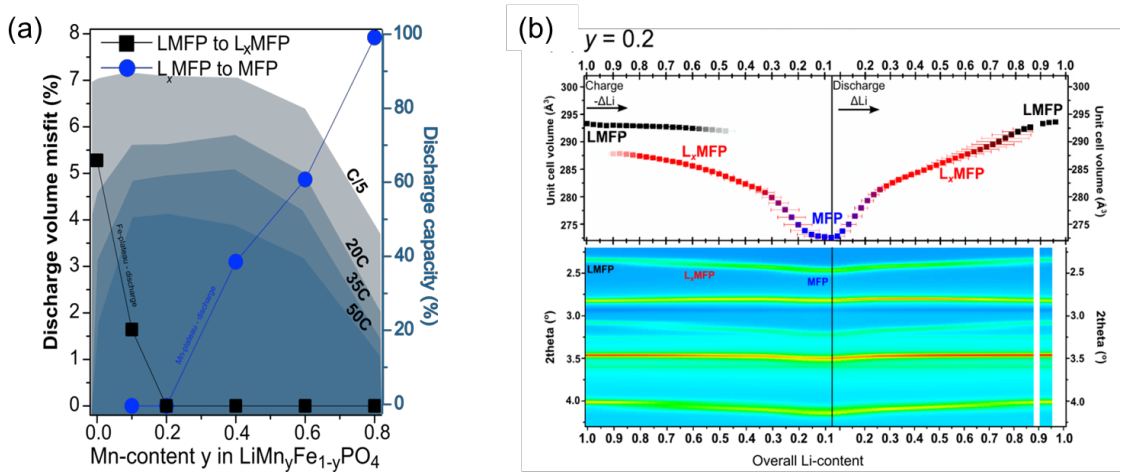

Figure 3 a) Volume misfit strain observed during operando discharge for LMFP, vs. Mn content. Shaded contours show the discharge capacity measured at C-rates from C/5 up to 50C. b) Unit cell dimensions for y = 0.2 sample during a charge/discharge cycle at C/10 rate. A small-strain first-order transition during charge is completely bypassed during discharge, producing a continuous solid solution transition. From ref. [18].

NaFePO$_4$ phospho-olivine:

Sodium-ion batteries are of much interest as an alternative to Li-ion due to the potentially lower cost of storage (i.e., $/kWh) associated with greater natural abundance of Na vs. Li. However, the energy density of Na-ion is typically lower for isostructural hosts due to the ~20% lower insertion potential of Na. Consequently, use of hosts based on low-cost transition metals such as Fe and Mn are essential if the cost advantages are to be realized. Sodium olivines are therefore of interest for much the same reasons as lithium olivines. However, pure NaFePO$_4$ is not stable in the olivine structure but instead forms maricite, which is largely electrochemically inactive. Nonetheless, the properties of metastable olivine NFP can be studied in samples prepared from LiFePO$_4$ by chemical delithiation followed by electrochemical sodiation[23]. In this project, NFP is prepared by using starting LiFePO$_4$ powders of ~50nm equivalent spherical particle size[24]. ICP analysis showed that the prepared NFP had less than 1% residual Li. This approach allows comparing phase behavior of NFP that is *morphologically identical* to the LFP and LMFP samples. Using the AMPIX *operando* cell for SR-PXD at APS, the olivine NFP phase behavior during electrochemical sodiation (discharge) and desodiation (charge) at C/20 galvanostatic rate was observed. Careful structure refinement led to the results shown in Figure 4, which shows the voltage vs. Na/Na$^+$ during initial sodiation (discharge) of the chemically delithiated starting olivine FePO$_4$ followed by a complete charge-discharge curve. The cell voltage shows hysteresis between discharge and charge, and exhibits a single characteristic voltage on discharge but two voltage "plateaus" on charge that suggest a pair of two-phase equilibria, followed by a continuously rising voltage in a single solid solution regime. Figure 4b shows the corresponding unit cell volumes of the highly sodiated Na$_{1-y}$FePO$_4$ ($0<y<\sim0.4$) and highly desodiated Na$_x$FePO$_4$ ($0<x<0.08$) olivines, which are the only crystalline phases detected. The unit cell volumes are approximately invariant during the first discharge (sodiation), suggesting a conventional first order transition. However, during the second charge (desodiation), the unit cell volume of the

NFP decreases following an S-shaped curve, and during the second discharge this S-shaped curve is approximately reversed. The difference in unit cell volume between the sodiated and desodiated coexisting olivine phases is large and variable, ranging from 16% to 10%, which is greater than known for any other olivine.

Additional insights arise upon quantifying the SR-PXD data for the absolute amount of each crystalline phase across the electrochemical cycles[24]. Figure 4c plots the relative amount of each olivine phase, and the total amount of crystalline phase, as a function of scan number. During first sodiation, the total crystalline fraction decreases to 60% of its initial value, and upon desodiation only about 90% of the crystalline content is recovered. From the second charge/discharge cycle, this behavior appears to be largely reversible. Clearly, one or more disordered phase must be created upon cycling. The presence of the disordered phase is confirmed by high-resolution TEM shown in Figure 5.

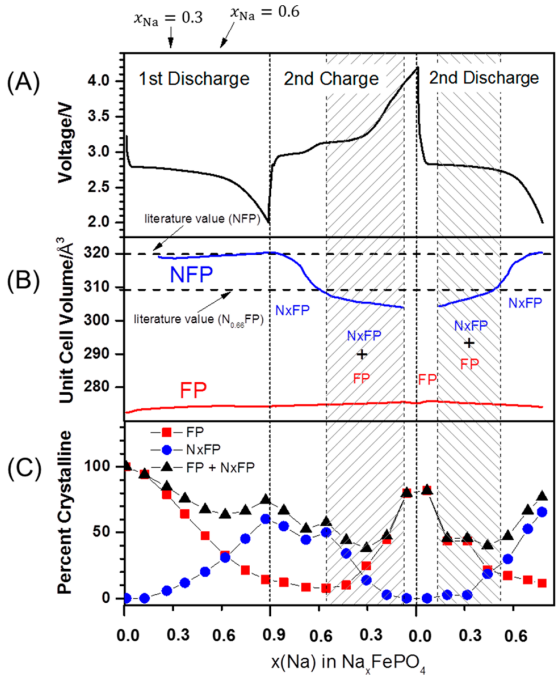

Figure 4. Operando cell results for olivine $NaFePO_4$ vs. Li/Li^+. (a) Reversible sodium insertion into chemically delithiated $LiFePO_4$ of 50nm average crystallite size at C/20 rate, reaching 90% of the theoretical capacity. Note difference in behavior between first insertion and subsequent cycle. (b) Unit cell volume for the highly sodiated and nearly desodiated olivine phases, and (c) Variation in individual and total crystalline phase content with electrochemical cycling. From ref. 24.

We propose that the observed disorder/amorphization occurs to accommodate the large induced transformation strains of 10-16 vol%. This represents a novel strain accommodation mechanism for battery materials. As a stark contrast from the more common mechanisms based on dislocation plasticity and fracture, the amorphous phase formation exhibits reversibility upon (de)sodiation and could potentially allow large transformation strain to be tolerated during charge/discharge without causing irreversible degradation to electrode structure and performance.

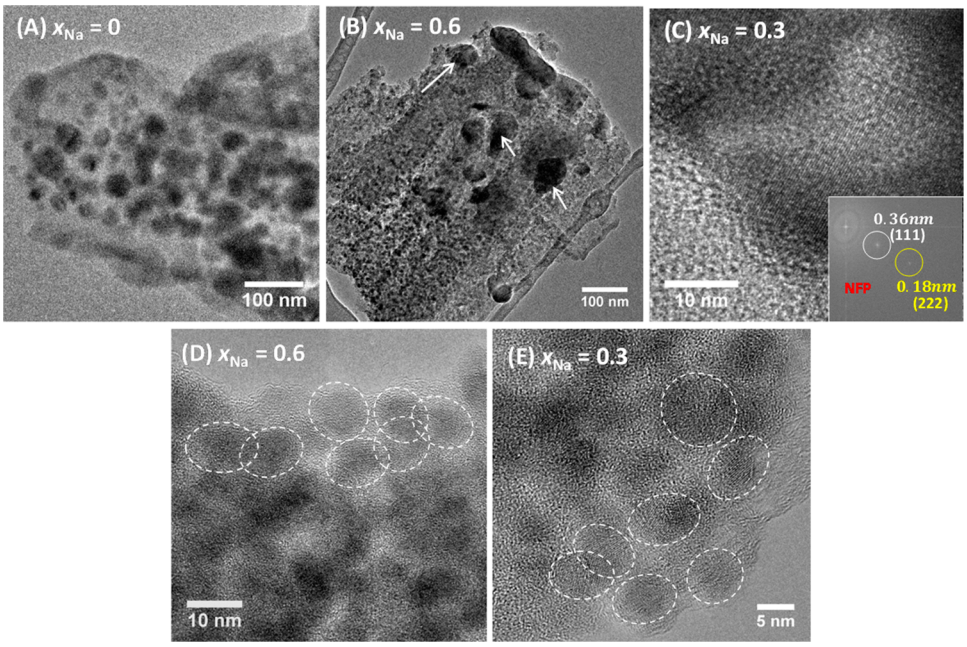

Figure 5 TEM images of 50-nm Na_xFePO_4 particles at different stages of sodiation. (A) Full delithiated 50-nm LFP particles at x_{Na} = 0. (B) Sodiation to x_{Na} = 0.6. Arrows indicate crystallites of the original size, which are more sparsely distributed. (C) Sodiation to x_{Na} = 0.3. The larger crystallites are identified to be either highly sodiated NFP or desodiated FP. (D, E) The material in between the larger nanocrystallites contains material exhibiting no distinct lattice fringes, corresponding to an amorphous phase. Small crystallites (circled regions) embedded in the amorphous phase are also observed to result from the transformation. From ref. [24].

II. Hybrid phase transition behavior resulting from kinetic competition of surface reaction and bulk diffusion

Many battery compounds undergo first-order phase transformations upon charge/discharge. The migration of phase boundary in intercalation compounds can be kinetically controlled by different rate-limiting steps include the bulk diffusion of ions inside electrode particles, the hopping of ions across the interface, and the (de)intercalation of ions across the particle surface. While bulk-diffusion-limited (BDL) and interface-source-limited phase boundary migration behaviors are well studied in other bulk materials, the fact that intercalation compounds are open systems (i.e. exchanging mass with environment) gives rise to an entirely new type of transformation kinetics, in which the phase boundary movement is controlled by how fast ions are inserted or extracted across the electrode/electrolyte interface. This surface-reaction-limited (SRL) growth mechanism has been predicted[25], but has not been reported for any intercalation compounds so far. Furthermore, it is also unknown whether the competition between surface reaction and other rate-limiting steps such as bulk diffusion can lead to new phase transition behavior and what is the implication for battery performance.

In collaboration with Dr. Song Jin's research group, we studied the phase boundary migration kinetics in $LiFePO_4$ through combined operando characterization and phase-field modeling[26]. Single-crystalline LFP micro-rods with long-axis grown along the [010] direction (Figure 6) were specifically synthesized to facilitate observation. We apply *operando* TXM-XANES imaging to visualize the electrochemical delithiation process in individual particles, see Figure 7. The first striking observation from the TXM images is that delithiation initiated on (100)/(001) instead of (010) particle surfaces, which suggests that the LFP particle has a non-negligible diffusion constant in the [100]/[001] direction. This is in contrast to the conventional belief that lithium diffusion is confined to one-dimensional [010] migration channels in LFP[27]. Through further comparison between the rate performance data from measurement and calculation, we confirm that the presence of only ~3% antisite defects, which are common in the synthesis of battery electrode materials, can induce the transition from 1D to isotropic Li diffusivity in LFP as predicted by DFP calculations[28]. A direct consequence of such behavior is that, against common belief, the (100) or (001) surfaces of LFP particles should be practically considered as active in the Li (de)intercalation process.

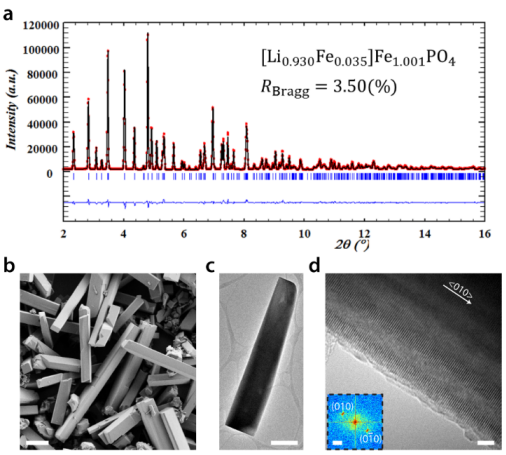

Figure 6 LFP microrod particles. a) XRD data. b) SEM image (scale bar 10 μm). c & d) low- and high-resolution TEM images (scale bar 1 μm and 5 nm, respectively). From ref. 26.

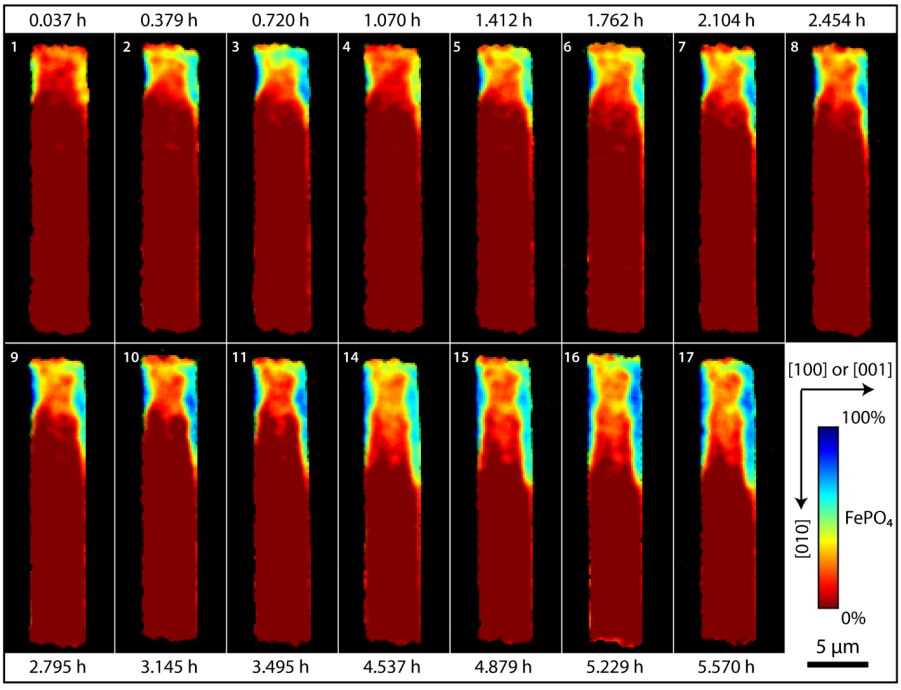

Figure 7. *Operando* TXM-XANES imaging of delithiation of a single-crystal $LiFePO_4$ microrod. 2D depth-averaged $FePO_4$ single-phase chemical maps (58 × 162 pixels; 1 pixel = ~160 nm) taken at different states of charge show the evolution of the phase state of a $LiFePO_4$ microrod along different crystallographic directions. The long-axis of the $LiFePO_4$ microrod is along [010] and its short-axis is along [100] or [001]. The "jet" color-scale corresponds to the fraction of the FP phase (red, 0% $FePO_4$; blue, 100% $FePO_4$). Scale bar is 5 μm. From ref. [26].

As a second prominent finding from the TXM results, we discovered that the fast growth rate of $FePO_4$ phase along [010] direction in the LFP microrod cannot be explained by bulk diffusion kinetics. Through detailed comparison of the experimental data against phase-field modeling (Figure 8), we conclude that the observed phase growth morphology results from a new hybrid phase boundary migration mode. In this mode, following its nucleation at particle surface upon (de)lithiation, the growth of the FP phase within the particle becomes kinetically limited by Li diffusion in the [100]/[001] direction but is controlled instead by surface reaction along [010] axis. The hybrid mode exhibits a qualitatively different scaling relation between transformed fraction and time ($f \propto t^{3/2}$) than the BDL ($f \propto t^{1/2}$) and SRL ($f \propto t$) modes.

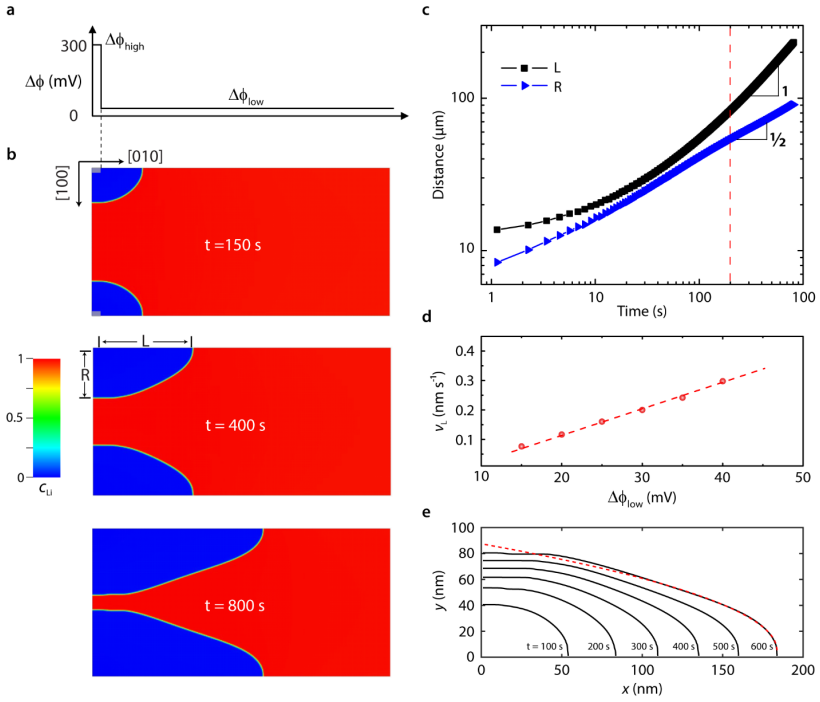

Figure 8. Phase-field simulation of delithiation in $LiFePO_4$. a) Overpotential applied on (100)/(001) surface. b) FP phase morphology (blue domains) at t = 150 s, 400 s and 800 s. c) Log-log plot of the dimensions of FP domain along [010] and [100]/[001] against delithiation time. d) Triple junction velocity obtained from phase-field simulation as a function of overpotential. e) Time evolution of phase boundary profiles, which can be described by a parabolic curve $y \propto \sqrt{L(t) - x}$. From ref. [26].

The existence of the hybrid phase transition mode is expected to be a general feature of intercalation compounds not unique to LFP. As shown in Figure 9, we suggest that there are three general kinetic regimes of phase transformations in intercalation compounds when interface reaction (or ion hopping across phase boundary) is facile and not a rate-limiting step. They include the SRL and BDL regimes as well as an intermediate hybrid regime. Phase transitions may switch from one to another kinetic regime upon changing diffusivity, applied overpotential $\Delta\phi$, and particle size along the Li intercalation direction. The existence of multiple kinetic modes presents additional complexity for accurately predicting the rate performance of intercalation compounds that undergo electrochemically-driven phase transformations.

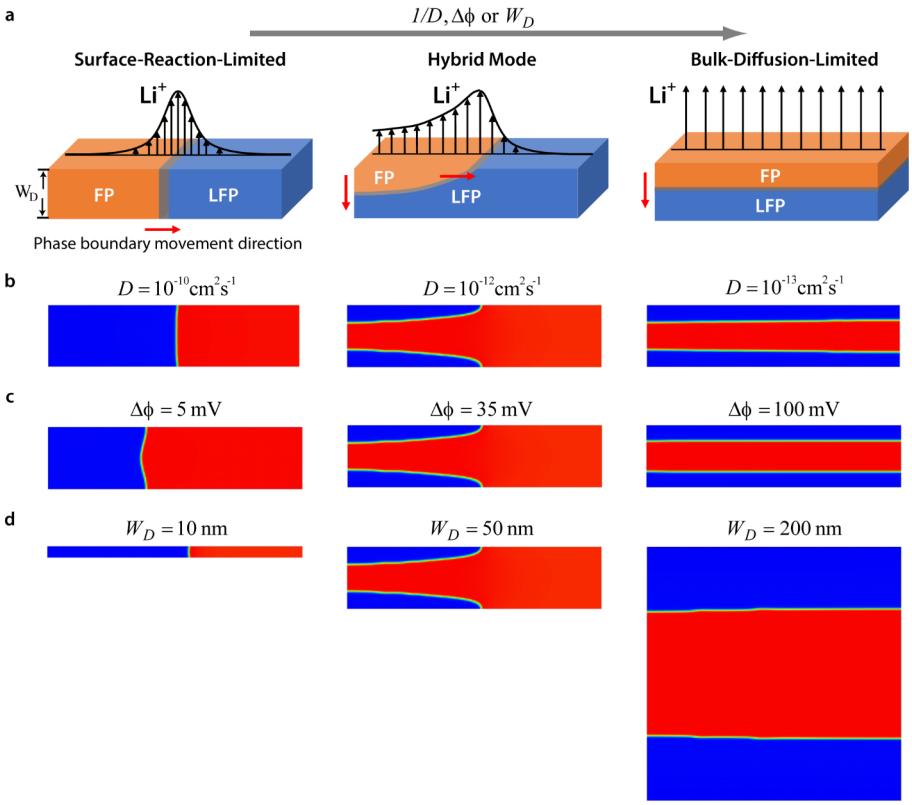

Figure 9 Kinetic regimes of phase transitions. a) Schematics of three kinetic regimes of phase boundary migration in intercalation compounds. Phase-field simulations of the transition from SRL to hybrid and then BDL boundary movement in $LiFePO_4$ upon b) decreasing Li diffusivity D, c) increasing overpotential $\Delta\phi$ and d) increasing particle thickness along the main Li intercalation direction W_D. An exchange current density of j_0 = 1 A m^{-2} and 2D Li diffusivity are used in all simulations. $\Delta\phi$ = 35 mV and W_D = 50 nm for simulations shown in b, $D = 10^{-12}$ cm^2 and W_D = 50 nm for simulations in c, and $D = 10^{-12}$ cm^2 s^{-1} and $\Delta\phi$ = 35 mV for simulations in d. From ref. [26].

III. Mesoscopic Phase Transition behavior in Secondary Electrode Particles

An important question we address in this project is how the nucleation and growth process of phase transition proceeds at the particle ensemble level in battery electrodes. Despite extensive studies on phase transition kinetics in $LiFePO_4$ and other battery compounds in general, the characteristics of phase transformation in realistic microstructures composed of ensembles of electrode particles remains poorly understood. In studying collective trans- formation behavior, simplified models are often assumed in which the particles are well-separated single crystallites that interact indirectly through ion exchange with the surrounding electrolyte. However, realistic electrodes, including those in commercial Li-ion batteries today, consist of microscale agglomerates (i.e., secondary particles) of smaller and often nanosized primary particles of the active material. As the primary particles within a secondary particle may strongly interact both electrochemically and mechanically during cycling, the phase transformation behavior of the agglomerate is critical to electrode performance and may differ significantly from that of stand-alone particles. The determination of mesoscopic transformation kinetics at the aggregate level thus has practical importance for designing and optimizing battery electrodes.

In collaboration with Dr. Yet-Ming Chiang's research group, systematic potentiostatic experiments were conducted and analyzed to probe the phase transformation kinetics in secondary particles of three well-known Li-ion battery cathodes: LFP, $LiMn_yFe_{1-y}PO_4$ (LMFP) olivines, and $Li_4Ti_5O_{12}$ spinel[29]. Experiments cover a wide range of overpotentials, varying transition-metal composition in the case of LMFP (to access different portions of the equilibrium phase diagram), particle size (for the olivines), and temperature. Figure 10 shows selected PITT data as a function of overpotential, composition, and particle size.

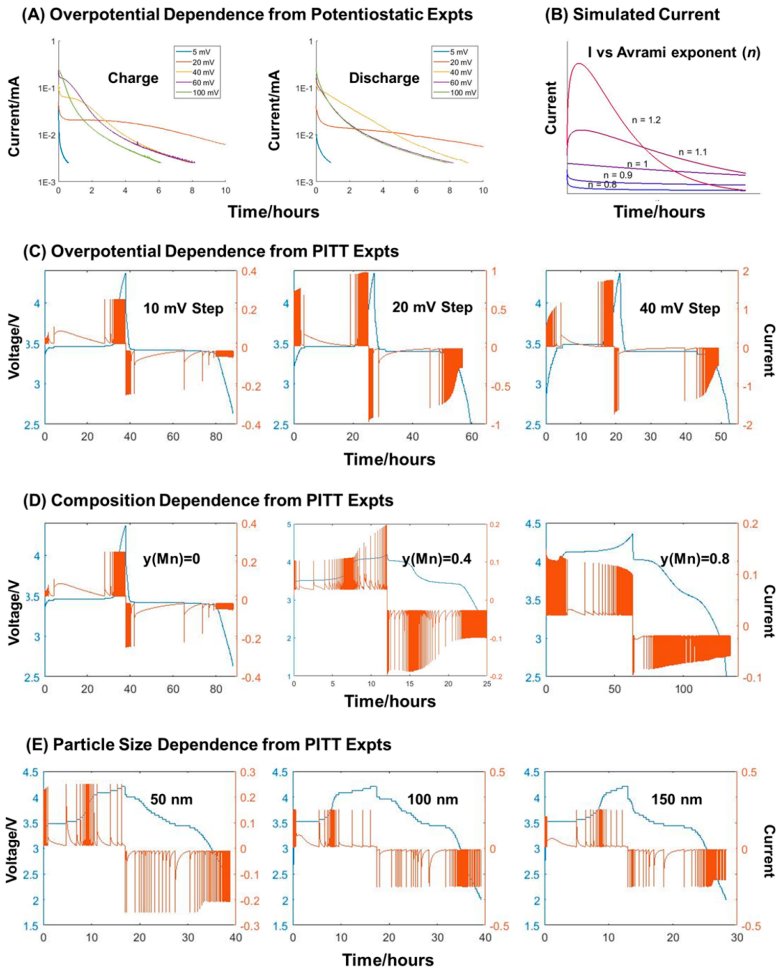

Figure 10 (A) Potentiostatic experiments in which a starting composition $Li_{0.5}FePO_4$ was charged or discharged at over(under)potential values of 5, 20, 40, 60, and 100 mV. (B) Transient current as a function of time predicted by the JMAK equation, for different Avrami exponents n. (C−E) Voltage (V) vs time and current (mA) vs time profiles from PITT experiments testing individual variables. (C) Varying overpotential. LFP of 50 nm equivalent spherical diameter is tested under voltage steps of 10, 20, and 40 mV. (D) Varying LMFP composition. LMFP of 50 nm equivalent spherical particle diameter and y(Mn) = 0, 0.4, and 0.8 are tested under 10 mV overpotential. (E) Varying primary particle size. LMFP (y(Mn) = 0.4) with equivalent spherical particle diameter of 50, 100, and 150 nm is tested under 40 mV overpotential. All experiments conducted at 20 °C. From ref. [29].

We analyzed the acquired PITT results with the Johnson-Mehl-Avrami-Kolmogolov (JMAK) model. While the JMAK equation is widely used for analyzing concurrent nucleation and growth kinetics in bulk materials and has been repeatedly applied to olivine cathodes in literature[30], we clarified for the first time why this analysis can still be valid for nanoparticulate systems even though the major assumptions underlying the JMAK equation (infinite system and homogeneous nucleation) appear to be no longer satisfied. Based on insights from structure characterization and simulation, we show that the JMAK equation should be interpreted as probing the nucleation and growth process within secondary particles that consist of a large number of nanoscale primary particles.

As a major outcome of the JMAK analysis, the Avrami exponent n can be generally expressed as $n = a + b*c$, where parameter a is related to nucleation kinetics (a=0, instantaneous nucleation; a = 1, constant nucleation rate), b represents the growth dimensionality and c is controlled by phase boundary migration mechanism (diffusion- vs interface-limited). By fitting the PITT data of various $LiMn_yFe_{1-y}PO_4$ samples with different Mn:Fe ratio and particle size under different overpotentials and temperatures, we observe that the Avrami exponent n systematically varies between 0.5 and 1.5, see Figure 11.

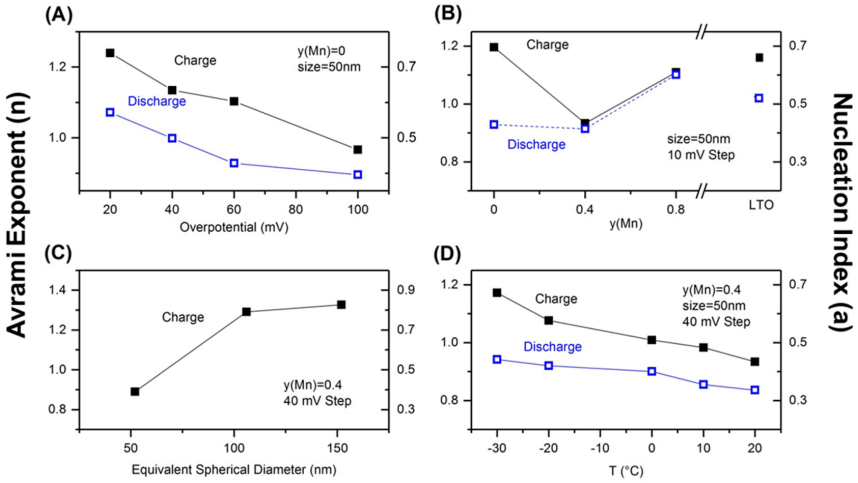

Figure 11 Avrami exponent (n) and nucleation index (a) as a function of A) overpotential for LFP secondary particles, B) compositions of LMFP and LTO, C) primary particle size for LMFP (y(Mn) = 0.4) secondary particles, D) temperature for LMFP (y(Mn) = 0.4) of 50 nm primary particle size. From ref. [29].

By assigning the parameters a, b and c to the obtained Avrami exponents in a self-consistent way, we obtain the following insights on the nucleation and growth process in the secondary particles:

1) Nucleation occurs through heterogeneous nucleation on two-dimensional particle surface followed by one-dimensional phase growth (i.e. b =1) into individual primary particles.
2) Phase boundary movement is controlled Li diffusion, i.e. c = 1/2.
3) Nucleation index a varies between 0.2 and 0.7; nucleation kinetics is modulated by particle size and composition, applied overpotential and operation temperature.

Based on the results, we propose that phase transitions in microsized secondary particles proceed through a hybrid mode previously discovered in LFP single crystals[26]. As illustrated in Figure 12a, the new phase displays fast two-dimensional growth on the internal surface of the agglomerates, while the rate-limiting step is the diffusion-controlled phase boundary movement in the surface normal direction, which accounts for the growth dimensionality of 1 from the JMAK interpretation. Such growth behavior is reproduced in our phase-field simulation of FP phase growth in a 19-particle aggregate under potentiostatic conditions (Figure 12b) by using a previously developed model for LFP[22].

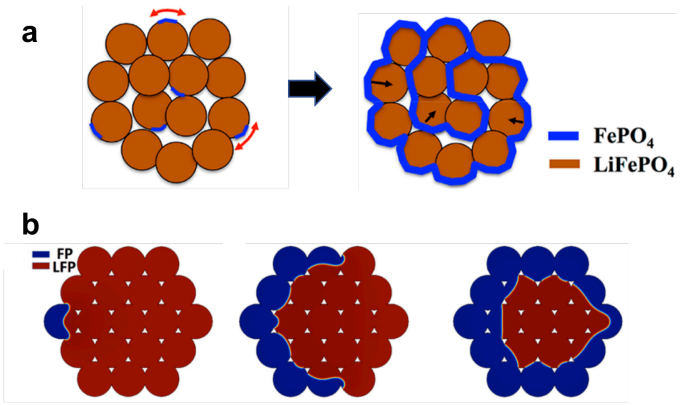

Figure 12 a) Schematic of the operation of the hybrid phase growth mechanism in a secondary particle. b) Snapshots from the phase-field simulation of hybrid-mode FP phase growth in a 19-particle LFP aggregate under a constant overpotential of 25 mV. (A) t = 100 s, (B) t = 200 s, (C) t = 1000 s. From ref. [29].

IV. Effect of electroplating stress on Li dendrite growth

Electrodeposition represents a broad category of phase transition phenomena in which materials transform between solution and solid phases under electromotive force. Recently, the development of unstable dendritic morphology during lithium electrodeposition receives considerable interest because it poses a critical challenge to the cycle life and safety of lithium metal anode, a key component in the next-generation rechargeable batteries[31-34]. While considerable progress has been made on mitigating Li dendrite growth through various approaches such as the development of electrolyte additives[35-37], artificial solid-electrolyte-interphase (SEI)s[38,39] and solid electrolytes[40-42], we still fall short of identifying a winning solution to completely address the dendrite problem. To a large degree, this is exacerbated by our incomplete understanding of the morphological instability mechanisms that operate during the electroplating of these metals.

In collaboration with Dr. Hanqing Jiang's research group at Arizona State University, we obtained a key insight to the lithium dendrite growth mechanism, namely, electroplating-induced residual stress in lithium provides the fundamental driving force for dendrite growth[43]. The generation of residual stress is a ubiquitous phenomenon in metal electroplating[44,45]. The morphology and root-growing behavior of Li filaments bear a striking similarity to the *stress-driven tin whisker growth*[46-49], a long-known phenomenon that can cause the critical failure of electronic devices. Extensive research has established that whiskers grow out of Sn surface in the presence of compressive stress[48]. However, the potential role of plating residual stress as a driving force for Li dendrite growth has received little attention. Equipped with the established understanding of Sn whisker growth[48], we found that Li electroplating provides favorable conditions for a stress-driven dendrite growth mechanism, which is absent in other metallic electrodeposition systems. They include: the surface passivation by SEI to prevent stress relaxation through the *uniform* creep of deposited Li; the extremely high room-temperature Li self-diffusivity ($\sim 10^{-15}$ m^2/s [50]), which enables whisker growth at a speed comparable to the plating

process. Motivated by the initial analysis, experiments[51] were conducted to prove: **(1)** Li plating generates compressive residual stress, **(2)** the compressive stress is responsible for Li filament growth, and **(3)** filamentary/mossy Li can be suppressed by releasing the plating stress.

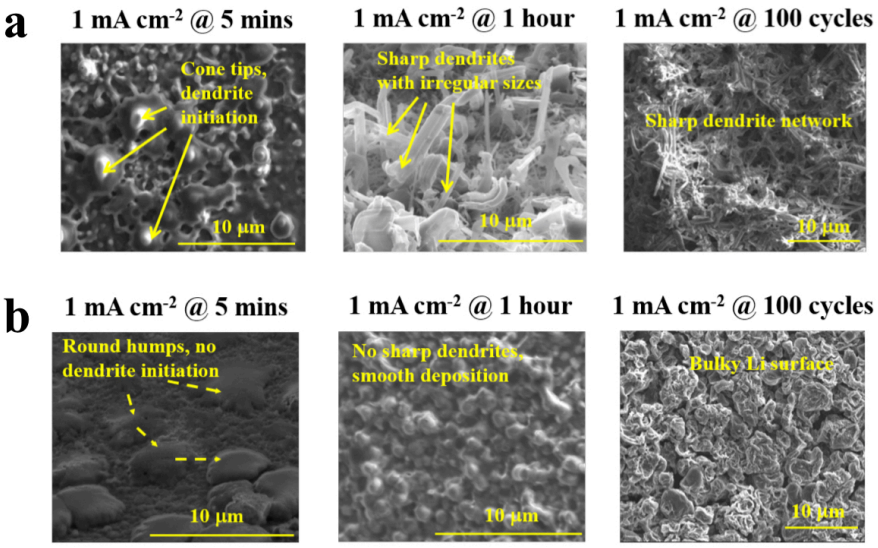

Figure 13. SEM images of a) Li plating morphology on hard Cu substrate, showing extensive dendrite formation, and b) Li plating morphology on soft current collector (Cu thin film on PDMS), showing dendrite-free growth. From ref. [43].

As illustrated in Figure 13, Li electrodeposition was performed on two types of substrates, i.e. "hard substrate" (thick Cu current collector) vs "soft substrate" (Cu thin film on poly(dimethylsiloxane) or PDMS). Without stress relief, plating on hard substrate at a current density of 1 mA cm^{-2} in carbonate electrolyte (1M $LiPF_6$ in DEC:EC:DMC) leads to Li filament initiation after only 5 minutes of plating, the formation of a dense filament "forest" after 1 hour, and dendrite network after 100 cycles (Figure 13a). In contrast, *in-situ* and *ex-situ* optical observations reveal that Li plating on soft substrate under otherwise the *same conditions* causes the Cu thin film to wrinkle (Figure 14). This result confirms that compressive stress develops in Li metal during plating, which is transferred to the soft substrate to induce wrinkling. The origin of compressive plating stress has been studied in various systems[44,45] and explained by the insertion of excessive atoms from electrolyte into grain boundaries (GBs). Compared with hard substrate, the wrinkling of Cu thin film on soft substrate releases the residual stress in deposited Li. Concomitantly, qualitatively different Li morphology is observed by *ex-situ* SEM (Figure 13b). A uniform distribution of round Li islands (or granular Li) forms on soft substrate after 5 minutes of charging. Exhibiting a typical Volmer-Webber growth mode, Li islands nucleate, grow, coalesce and form a continuous Li film upon further deposition, and no Li whiskers are seen. This result convincingly demonstrates that reducing plating stress can suppress filamentary/mossy Li growth by eliminating its driving force.

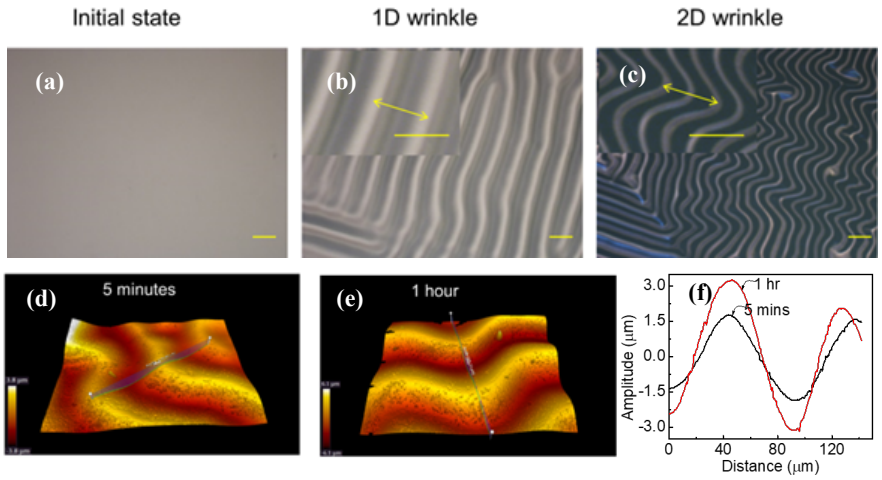

Figure 14 (a-c) *In-situ* optical images of soft substrate wrinkling morphology. Scale bar is 100 μm. (d-f) Surface profile of Cu film after Li plating by *ex-situ* profilometry measurement. From ref. ref. [43].

We proposed a stress-driven filament growth model[43] to interpret the experiments. Based on the prevailing understanding of tin whisker growth[48,52], the model assumes that filaments nucleate from surface grains and are "pushed out" by a localized diffusional creep process as shown in Figure 15. Because the filament is covered by SEI, which slows down Li deposition onto its sides and top, filament growth is mainly achieved by stress-induced Li flux added to its base. The predicted filament growth rate on hard substrate is consistent with the SEM measurement[43], and the model also satisfactorily explains the absence of Li filaments on soft substrate.

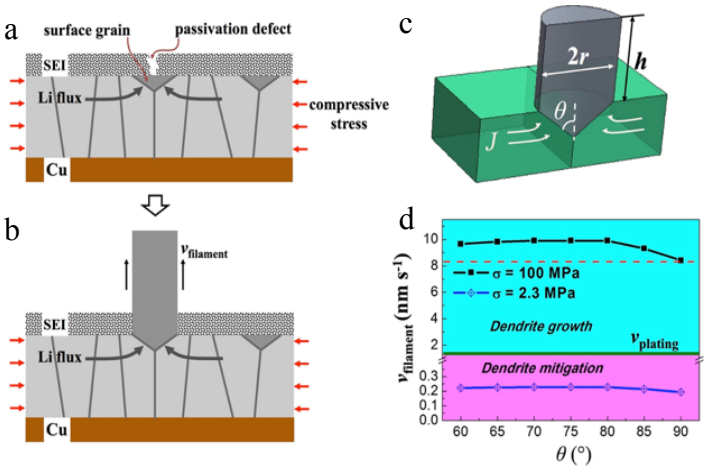

Figure 15 a,b. Stress-driven Li filament growth model. d. Calculated Li filament growth rate based on the geometry in c. From ref. ref. [43].

Furthermore, a phase-field model was developed to simulate the filamentary growth morphology. In addition to the mass conservation governing equation that considers stress-induced mass flux, the model uses a multi-order-parameter formulation[53] to describe grain

evolution and set a non-zero eigen-strain for grain boundaries in the mechanical equilibrium equation to model the generation of compressive stress. As shown in Figure 16, the simulation reproduces the stress-driven growth of a Li surface grain into filament and correctly captures its root growing behavior, as can be seen by the mass flux direction (black arrows) in Figure 16c.

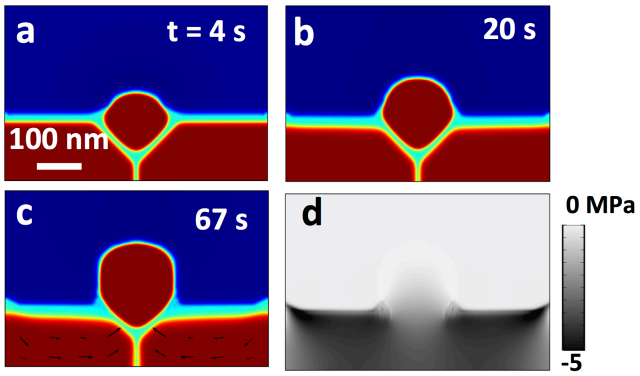

Figure 16 a) – c) PFM simulation of a root-growing Li surface grain under a compressive stress of 5 MPa. Arrows in c) represent Li flux. d) Hydrostatic stress distribution in the Li layer.

Journal Publications Resulting from this Project

[1] K. Xiang, K. Yang, W.C. Carter, M. Tang, Y.-M. Chiang, "Mesoscopic Phase Transition Kinetics in Secondary Particles of Electrode-Active Materials in Lithium-Ion Batteries", Chemistry of Materials 30, 4216 (2018).

[2] L. Cai, M. J. Shearer, Y. Zhao, Z. Hu, F. Wang, Y. Zhang, K. W. Eliceiri, R. J. Hamers, W. Yan, S. Wei, M. Tang, and S. Jin, "Chemically Derived Kirigami of WSe_2", Journal of the American Chemical Society 140, 35 (2018).

[3] Q. Meng, L. Wu, D. O. Welch, M. Tang and Y. Zhu, "Non-uniform Stress-free Strains in a Spherically Symmetrical Nanosized Particle and its Applications to Lithium-ion Batteries", Scientific Reports 8, 4936 (2018).

[4] X. Wang, W. Zeng, L. Hong, W. Xu, H. Yang, F. Wang, H. Duan, M. Tang, and H. Jiang, "Stress-Driven Lithium Dendrite Growth Mechanism and Dendrite Mitigation by Electroplating on Soft Substrates", Nature Energy 3, 227 (2018).

[5] L. Hong, L. Li, Y.-K. Chen-Wiegart, J. Wang, F. Wang, K. Xiang, L. Gan, W. Li, F. Meng, J. Wang, Y.-M. Chiang, S. Jin, M. Tang, "2D Li Diffusion Behavior and Probable Hybrid Phase Transformation Kinetics in Olivine Lithium Iron Phosphate", Nature Communications 8, 1194 (2017).

[6] J. Liu, B. Ludwig, Y. Liu, Z. Zheng, F. Wang, M. Tang, J. Wang, J. Wang, H. Pan, Y. Wang,"Scalable Dry Printing Manufacturing to Enable Long Life and High Energy Lithium-Ion Batteries", Advanced Materials Technology 2, 1700106 (2017).

[7] K. Xiang, W. Xing, D. B. Ravnsbæk, L. Hong, M. Tang, Z. Li, K. M. Wiaderek, O. J. Borkiewicz, K. W. Chapman, P. J. Chupas, Y.-M. Chiang (2017), "Accommodating High Transformation Strains in Battery Electrodes via Formation of Nanoscale Intermediate Phases: Operando Investigation of Olivine $NaFePO_4$", Nano Letters, 17, 1696.

[8] Li, B., Gong, Y. J., Hu, Z. L., Brunetto, G., Yang, Y. C., Ye, G. L., Zhang, Z. H., Lei, S. D., Jin, Z. H., Bianco, E., Zhang, X., Wang, W. P., Lou, J., Galvao, D. S., Tang, M., Yakobson, B. I., Vajtai, R., Ajayan, P. M. (2016), "Solid-Vapor Reaction Growth of Transition-Metal Dichalcogenide Monolayers". Angewandte Chemie-International Edition 55, 10656.

[9] Wu, J. J., Hu, Z. L., Jin, Z. H., Lei, S. D., Guo, H., Chatterjee, K., Zhang, J., Yang, Y. C., Li, B., Liu, Y., Lai, J. W., Vajtai, R., Yakobson, B., Tang, M., Lou, J., Ajayan, P. M.* (2016), "Spiral Growth of SnSe2 Crystals by Chemical Vapor Deposition." Advanced Materials Interfaces 3, 16.

[10] D. B. Ravnsbaek, K. Xiang, W. Xing, O. J. Borkiewicz, K. M. Wiaderek, P. Gionet, K. W. Chapman, P. J. Chupas, M. Tang, Y.-M. Chiang (2016), "Engineering the Transformation Strain in $LiMn_yFe_{1-y}PO_4$ Olivines for Ultrahigh Rate Battery Cathodes", *Nano Letters* 16, 2375.

[11] "Solvent-directed sol-gel assembly of 3-dimensional graphene-tented metal oxides and strong synergistic disparities in lithium storage", J. Ye, Y. An, E. Montalvo, P. G. Campbell, M. A. Worsley, I. C. Tran, Y. Liu, B. C. Wood, J. Biener, H. Jiang, M. Tang, Y. M. Wang, *Journal of Materials Chemistry* 4, 4032 (2016).

[12] "Solid−Liquid Self-Adaptive Polymeric Composite", P. Dong, A. C. Chipara, P.

Loya, Y. Yang, L. Ge, S. Lei, B. Li, G. Brunetto, L. D. Machado, L. Hong, Q. Wang, B. Yang, H. Guo, E. Ringe, D. S. Galvao, R. Vajtai, M. Chipara, M. Tang, J. Lou, P. M. Ajayan, *ACS Applied Materials & Interfaces* 8, 2142 (2016). **DOI:** 10.1021/acsami.5b10667

[13] "Defects, Entropy, and the Stabilization of Alternative Phase Boundary Orientations in Battery Electrode Particles", T. Heo, M. Tang, L.-Q. Chen, B. C. Wood, *Advanced Energy Materials* 6, 1501759 (2016). DOI: 10.1002/aenm.201501759

[14] "A Mechanism of Defect-Enhanced Phase Transformation Kinetics in Lithium Iron Phosphate", L. Hong, K. Yang and M. Tang, under review.

References

1 Limthongkul, P., Jang, Y.-I., Dudney, N. J. & Chiang, Y.-M. Electrochemically-driven solid-state amorphization in lithium-silicon alloys and implications for lithium storage. *Acta Materialia* **51**, 1103-1113, doi:10.1016/s1359-6454(02)00514-1 (2003).

2 Meethong, N., Huang, H.-Y. S., Carter, W. C. & Chiang, Y.-M. Size-Dependent Lithium Miscibility Gap in Nanoscale Li[sub 1−x]FePO[sub 4]. *Electrochemical and Solid-State Letters* **10**, A134, doi:10.1149/1.2710960 (2007).

3 Yamada, A. *et al.* Room-temperature miscibility gap in LixFePO4. *Nat Mater* **5**, 357-360, doi:10.1038/nmat1634 (2006).

4 Gibot, P. *et al.* Room-temperature single-phase Li insertion/extraction in nanoscale Li(x)FePO4. *Nat Mater* **7**, 741-747, doi:10.1038/nmat2245 (2008).

5 Ichitsubo, T. *et al.* What determines the critical size for phase separation in LiFePO4 in lithium ion batteries? *Journal of Materials Chemistry A* **1**, 14532-14537, doi:10.1039/c3ta13122j (2013).

6 Sharma, N. *et al.* Direct evidence of concurrent solid-solution and two-phase reactions and the nonequilibrium structural evolution of LiFePO4. *J Am Chem Soc* **134**, 7867-7873, doi:10.1021/ja301187u (2012).

7 Liu, H. *et al.* Batteries. Capturing metastable structures during high-rate cycling of LiFePO(4) nanoparticle electrodes. *Science* **344**, 1252817, doi:10.1126/science.1252817 (2014).

8 Zhang, X. *et al.* Rate-induced solubility and suppression of the first-order phase transition in olivine LiFePO4. *Nano Lett* **14**, 2279-2285, doi:10.1021/nl404285y (2014).

9 Hess, M., Sasaki, T., Villevieille, C. & Novak, P. Combined operando X-ray diffraction-electrochemical impedance spectroscopy detecting solid solution reactions of LiFePO4 in batteries. *Nat Commun* **6**, 8169, doi:10.1038/ncomms9169 (2015).

10 Lim, J. *et al.* Origin and hysteresis of lithium compositional spatiodynamics within battery primary particles. *Science* **353**, 566-571 (2016).

11 Meethong, N. *et al.* Electrochemically Induced Phase Transformation in Nanoscale Olivines Li1-xMPO4 (M = Fe, Mn). *Chemistry of Materials* **20**, 6189-6198 (2008).

12 Aurbach, D., Zinigrad, E., Cohen, Y. & Teller, H. A short review of failure mechanisms of lithium metal and lithiated graphite anodes in liquid electrolyte solutions. *Solid State Ionics* **148**, 405-416 (2002).

13 Takehara, Z. Future prospects of the lithium metal anode. *Journal of Power Sources* **68**, 82-86 (1997).

14 Kim, H. *et al.* Metallic anodes for next generation secondary batteries. *Chemical Society Reviews* **42**, 9011-9034 (2013).

15 Xu, W. *et al.* Lithium metal anodes for rechargeable batteries. *Energy Environ. Sci.* **7**, 513-537, doi:10.1039/c3ee40795k (2014).

16 An, Y. H. *et al.* Mitigating mechanical failure of crystalline silicon electrodes for lithium batteries by morphological design. *Physical Chemistry Chemical Physics* **17**, 17718-17728 (2015).

17 Ye, J. C. *et al.* Enhanced lithiation and fracture behavior of silicon mesoscale pillars via atomic layer coatings and geometry design. *Journal of Power Sources* **248**, 447-456, doi:10.1016/j.jpowsour.2013.09.097 (2014).
18 Ravnsbaek, D. B. *et al.* Engineering the Transformation Strain in LiMnyFe1-yPO4 Olivines for Ultrahigh Rate Battery Cathodes. *Nano Letters* **16**, 2375-2380 (2016).
19 Malik, R., Zhou, F. & Ceder, G. Phase diagram and electrochemical properties of mixed olivines from first-principles calculations. *Physical Review B* **79**, doi:10.1103/PhysRevB.79.214201 (2009).
20 Yamada, A., Kudo, Y. & Liu, K. Y. Phase diagram of Li-x(MnyFe1-y)PO4 (0 <= x, y <= 1). *Journal of the Electrochemical Society* **148**, A1153-A1158 (2001).
21 Ravnsbaek, D. B. *et al.* Extended solid solutions and coherent transformations in nanoscale olivine cathodes. *Nano Lett* **14**, 1484-1491, doi:10.1021/nl404679t (2014).
22 Tang, M., Belak, J. F. & Dorr, M. R. Anisotropic Phase Boundary Morphology in Nanoscale Olivine Electrode Particles. *J Phys Chem C* **115**, 4922-4926 (2011).
23 Gaubicher, J. *et al.* Abnormal operando structural behavior of sodium battery material: Influence of dynamic on phase diagram of Na FePO4. *Electrochemistry Communications* **38**, 104-106, doi:10.1016/j.elecom.2013.11.017 (2014).
24 Xiang, K. *et al.* Accommodating High Transformation Strains in Battery Electrodes via the Formation of Nanoscale Intermediate Phases: Operando Investigation of Olivine NaFePO4. *Nano Letters* **17**, 1696-1702 (2017).
25 Singh, G. K., Ceder, G. & Bazant, M. Z. Intercalation dynamics in rechargeable battery materials: General theory and phase-transformation waves in LiFePO4. *Electrochimica Acta* **53**, 7599-7613, doi:10.1016/j.electacta.2008.03.083 (2008).
26 Hong, L. *et al.* 2D Li Diffusion Behavior and Probable Hybrid Phase Transformation Kinetics in Olivine Lithium Iron Phosphate. *Nature Communications* **8**, 1194 (2017).
27 Morgan, D., Van der Ven, A. & Ceder, G. Li Conductivity in Li[sub x]MPO[sub 4] (M = Mn, Fe, Co, Ni) Olivine Materials. *Electrochemical and Solid-State Letters* **7**, A30, doi:10.1149/1.1633511 (2004).
28 Malik, R., Burch, D., Bazant, M. & Ceder, G. Particle size dependence of the ionic diffusivity. *Nano Lett* **10**, 4123-4127, doi:10.1021/nl1023595 (2010).
29 Xiang, K., Yang, K. Q., Carter, W. C., Tang, M. & Chiang, Y. M. Mesoscopic Phase Transition Kinetics in Secondary Particles of Electrode-Active Materials in Lithium-Ion Batteries. *Chemistry of Materials* **30**, 4216-4225, doi:10.1021/acs.chemmater.7b05407 (2018).
30 Oyama, G., Yamada, Y., Natsui, R.-i., Nishimura, S.-i. & Yamada, A. Kinetics of Nucleation and Growth in Two-Phase Electrochemical Reaction of LixFePO4. *The Journal of Physical Chemistry C* **116**, 7306-7311, doi:10.1021/jp300085n (2012).
31 Albertus, P., Babinec, S., Litzelman, S. & Newman, A. Status and challenges in enabling the lithium metal electrode for high-energy and low-cost rechargeable batteries. *Nature Energy* **3**, 16-21 (2018).
32 Guo, Y. P., Li, H. Q. & Zhai, T. Y. Reviving Lithium-Metal Anodes for Next-Generation High-Energy Batteries. *Advanced Materials* **29** (2017).

33 Lin, D. C., Liu, Y. Y. & Cui, Y. Reviving the lithium metal anode for high-energy batteries. *Nature Nanotechnology* **12**, 194-206 (2017).
34 Higashi, S., Lee, S. W., Lee, J. S., Takechi, K. & Cui, Y. Avoiding short circuits from zinc metal dendrites in anode by backside-plating configuration. *Nature Communications* **7** (2016).
35 Li, W. Y. *et al.* The synergetic effect of lithium polysulfide and lithium nitrate to prevent lithium dendrite growth. *Nature Communications* **6** (2015).
36 Ding, F. *et al.* Dendrite-Free Lithium Deposition via Self-Healing Electrostatic Shield Mechanism. *Journal of the American Chemical Society* **135**, 4450-4456 (2013).
37 Qian, J. F. *et al.* High rate and stable cycling of lithium metal anode. *Nature Communications* **6** (2015).
38 Choudhury, S. *et al.* Electroless Formation of Hybrid Lithium Anodes for Fast Interfacial Ion Transport. *Angew Chem Int Edit* **56**, 13070-13077 (2017).
39 Yan, K. *et al.* Ultrathin Two-Dimensional Atomic Crystals as Stable Interfacial Layer for Improvement of Lithium Metal Anode. *Nano Letters* **14**, 6016-6022 (2014).
40 Monroe, C. & Newman, J. The impact of elastic deformation on deposition kinetics at lithium/polymer interfaces. *J. Electrochem. Soc.* **152**, A396-A404 (2005).
41 Murugan, R., Thangadurai, V. & Weppner, W. Fast lithium ion conduction in garnet-type Li7La3Zr2O12. *Angew Chem Int Edit* **46**, 7778-7781 (2007).
42 Kim, K. H. *et al.* Characterization of the interface between LiCoO2 and Li7La3Zr2O12 in an all-solid-state rechargeable lithium battery. *Journal of Power Sources* **196**, 764-767 (2011).
43 Wang, X. *et al.* Stress-Driven Lithium Dendrite Growth Mechanism and Dendrite Mitigation by Electroplating on Soft Substrates. *Nature Energy* **3**, 227-235 (2018).
44 Chason, E. *et al.* Understanding Residual Stress in Electrodeposited Cu Thin Films. *Journal of the Electrochemical Society* **160**, D3285-D3289 (2013).
45 Shin, J. W. & Chason, E. Compressive stress generation in sn thin films and the role of grain boundary diffusion. *Phys Rev Lett* **103**, 056102, doi:10.1103/PhysRevLett.103.056102 (2009).
46 Frank, F. C. On Tin Whiskers. *Philosophical Magazine* **44**, 854-860 (1953).
47 Galyon, G. T. Annotated tin whisker bibliography and anthology. *Ieee T Electron Pack* **28**, 94-122 (2005).
48 Chason, E., Jadhav, N., Pei, F., Buchovecky, E. & Bower, A. Growth of whiskers from Sn surfaces: Driving forces and growth mechanisms. *Progress in Surface Science* **88**, 103-131, doi:10.1016/j.progsurf.2013.02.002 (2013).
49 *Mitigating Tin Whisker Risks: Theory and Practice*. (Wiley, 2016).
50 Wieland, O. & Carstanjen, H. D. Measurement of the low-temperature self-diffusivity of lithium by elastic recoil detection analysis. *Defect Diffus Forum* **194-1**, 35-41 (2001).
51 Wang, X. *et al.* Stress-driven lithium dendrite growth mechanism and dendrite mitigation by electroplating on soft substrates. *Nature Energy* **3**, 227-235, doi:10.1038/s41560-018-0104-5 (2018).

52 Sarobol, P., Blendell, J. E. & Handwerker, C. A. Whisker and hillock growth via coupled localized Coble creep, grain boundary sliding, and shear induced grain boundary migration. *Acta Materialia* **61**, 1991-2003, doi:10.1016/j.actamat.2012.12.019 (2013).
53 Fan, D. & Chen, L. Q. Computer simulation of grain growth using a continuum field model. *Acta Materialia* **45**, 611-622 (1997).